BMC Medical Imaging

RESEARCH

Open Access

CT-based radiomics models using intralesional and different perilesional signatures in predicting the microvascular density of hepatic alveolar echinococcosis

Juan Hou[1], Simiao Zhang[1], Shouxian Li[1], Zicheng Zhao[2], Longfei Zhao[2], Tieliang Zhang[1] and Wenya Liu[1*]

Abstract

Objectives To evaluate the performance of CT-based intralesional combined with different perilesional radiomics models in predicting the microvascular density (MVD) of hepatic alveolar echinococcosis (HAE).

Methods This study retrospectively analyzed preoperative CT data from 303 patients with HAE confirmed by surgical pathology (MVD positive, $n=182$; MVD negative, $n=121$). The patients were randomly divided into the training cohort ($n=242$) and test cohort ($n=61$) at a ratio of 8:2. The radiomics features were extracted from CT images on the portal vein phase. Four radiomics models were constructed based on gross lesion volume (GLV), gross combined 10 mm perilesional volume ($GPLV_{10mm}$), gross combined 15 mm perilesional volume ($GPLV_{15mm}$) and gross combined 20 mm perilesional volume ($GPLV_{20mm}$). The best radiomics signature model and clinical features were combined to establish a nomogram. Receiver operating characteristic curve (ROC) and decision curve analysis (DCA) were used to evaluate the predictive performance of models.

Results Among the four radiomics models, the $GPLV_{20mm}$ model performed the highest prediction performance with the area under the curves (AUCs) in training cohort and test cohort was 0.876 and 0.802, respectively. The AUC of the clinical model was 0.753 in the training cohort and 0.699 in the test cohort. The AUC of the nomogram model based clinical and $GPLV_{20mm}$ radiomic signatures was 0.922 in the training cohort and 0.849 in the test cohort. The DCA showed that the nomogram had greater benefits among the three models.

Conclusion CT-based $GPLV_{20mm}$ radiomics model can better predict MVD of HAE. The nomogram model showed the best predictive performance.

Keywords Hepatic alveolar echinococcosis, Computed tomography, Radiomics, Microvascular density, Machine learning

*Correspondence:
Wenya Liu
13999202977@163.com
[1]Imaging Center, First Affiliated Hospital of Xinjiang Medical University, Urumqi 830011, Xinjiang, China
[2]Canon Medical Systems (China), Beijing 100015, China

Introduction

Hepatic alveolar echinococcosis (HAE) is a potentially fatal zoonosis caused by the cestode Echinococcus multilocularis, and predominantly endemic in pastoral regions [1]. Due to its tumor-like growth, HAE has a high morbidity and mortality burden with a 10-year fatality rate of 94% in untreated or inadequately managed patients [2]. The primary treatment of HAE is operative intervention, yet preoperative evaluation of the lesion is essential to determine the feasibility of surgery and to optimize the surgical strategy [3]. The therapeutic goal of HAE is complete removal and killing of hydatid bodies, that is, to render it biologically inactive. Assessment of the bioactivity of the lesions of HAE is crucial to decide the therapeutic strategy and anti-infective drug withdrawal [4]. Studies have shown that the peripheral infiltration zone of HAE lesions has a rich microcirculation similar to that around malignant tumors, which is the active part of HAE lesions and can indirectly reflect the biological activity of worms [5]. Therefore, accurately assessing the MVD of HAE is an important means to evaluate its bioactivity and can provide an important basis for informing clinical treatment decisions and evaluating therapeutic outcomes.

Imaging examination is an important means of preoperative diagnosis and assessment of disease condition and curative effect of HAE. The gold standard for the judgment of the peripheral infiltration zone and bioactivity of HAE is the pathological microvascular density (MVD) in the peripheral area of the lesion, which cannot be morphologically demonstrated by conventional imaging [6]. Several functional imaging modalities, such as fluorodeoxyglucose positron-emission tomography (FDG-PET), contrast-enhanced ultrasound (CEUS), CT perfusion imaging, and quantitative dual-energy CT, have shown promise in evaluating the MVD and bioactivity of HAE lesions [6–8]. However, due to the medical conditions and economic constraints, functional imaging methods are difficult to popularize in the pastoral areas where HAE is prevalent. With the rapid development of machine learning-based radiomics, researchers have found new possibilities in quantitative assessment of the MVD and bioactivity of HAE lesions [9–11]. Previous studies mostly focused on the extraction of radiomics features within the gross lesion volume. According to the characteristics of chronic outward aggressive growth of HAE, we supposed that the perilesional tissue had a microenvironment more representative of its MVD and bioactivity.

The aim of this study is to construct radiomics models to predict the MVD of HAE based on features extracted from the intralesional and different perilesional regions of HAE, and to find out the best prediction model. Additionally, a visualized nomogram model were constructed with the best radiomics model signature and clinical features to provide a more comprehensive and accurate evaluation for clinical diagnosis and treatment.

Materials and methods

Patients

This retrospective study was approved by the institutional Ethics Committee of the First Affiliated Hospital of Xinjiang Medical University (No. K202312-38) and was conducted in accordance with the 1964 Helsinki Declaration and its later amendments or comparable ethical standards. The informed consent was waived as a retrospective study. From January 2012 to December 2023, 467 patients diagnosed with HAE from the First Affiliated Hospital of Xinjiang Medical University were collected. The inclusion criteria were as follows: (1) the MVD of HAE lesions have been pathologically determined; (2) contrast-enhanced abdominal CT images were obtained within 2 weeks before surgery; (3) CT images were met the diagnostic requirements. The exclusion criteria were as follows: (1) clinicopathological record was incomplete; (2) presence of other malignant tumors; (3) preoperative interventional therapy affected the images; (4) the lesion edges were not clearly identifiable for segmentation.

Finally, a total of 303 patients were enrolled. All patients were randomly divided into the training cohort ($n = 242$) and the test cohort ($n = 61$) in a ratio of 8:2 (Fig. 1; Table 1). There were 13 features were screened in the preliminary experiment, and the sample size was sufficient according to the 10 events per variable rule.

Pathological diagnosis of MVD and clinical feature selection

Paraffin sections containing HAE lesions and surrounding normal liver tissue were prepared into 4 mm sections. Hbematoxylin-eosin staining and immunohistochemical staining were performed [12]. The MVD count was performed by two trained pathologist with the double-blind method. With reference to Weidner's method, the "hot spot" of microvascular concentration was first found under low magnification microscope (×40), and then MVD was counted under high magnification microscope (×200) to calculate the mean value as the final MVD [13]. The MVD > 15 was considered positive [14]. Of the 303 patients included in this study, 182 were classified as positive, while 121 were classified as negative.

Clinical features included age, sex, body mass index (BMI), location, number, diameter and calcification type of lesion, some relevant laboratory tests. The calcification type of lesion follows the following criteria: (1) Type A: spotty, minimal calcification with no obvious or discontinuous calcification, or visible spotty calcification that is more limited; (2) Type B: cartographic, moderate calcification, with continuous cartographic calcification in

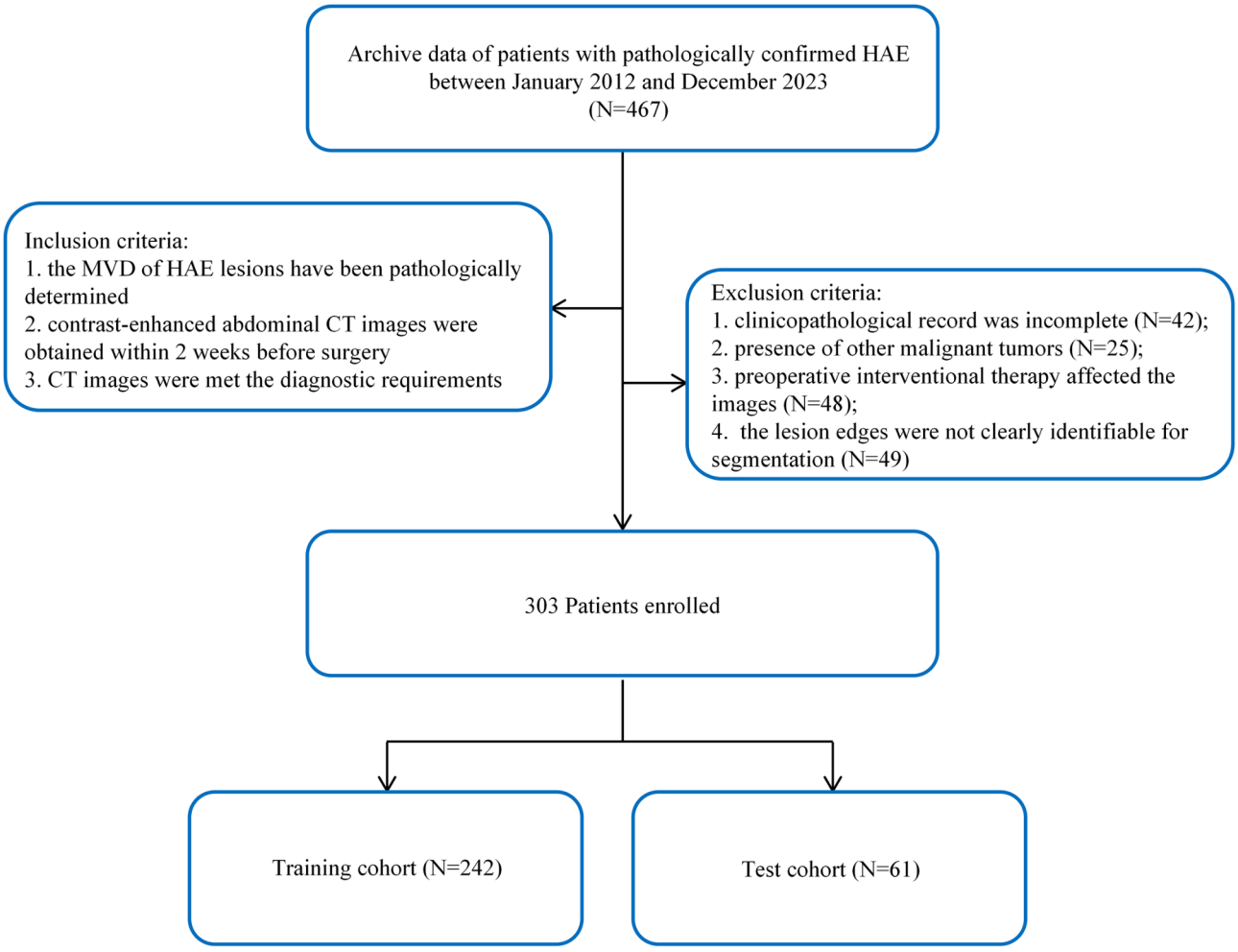

Fig. 1 Flowchart of the study subjects based on inclusion and exclusion criteria

the middle and peripheral zones, with or without central speckled calcification; (3) Type C: large, flaky calcifications, predominantly located in the lateral lesion near the hepatic margin. Laboratory tests mainly include blood routine and liver function related indicators, such as white blood cells (WBC), neutrophils count (NE), lymphocyte count (Lym), aspartate aminotransferase (AST), alanine aminotransferase (ALT), fibrinogen (Fib), platelet count (PLT), creatinine (Crea), total bilirubin (TBIL). Univariate and multivariate logistic regression were used to analyze the clinical features and to select out independent predictors for clinical model construction.

CT image acquisition

All enrolled patients have taken preoperative CT examinations with a multidetector CT system with the following two scanners: Aquilion ONE Genesis Edition (Canon Medical Systems, Japan), GE Discovery HD750 (GE Medical Systems, Milwaukee, WI, USA). During scanning, patients were acquired in the supine position and in inspiratory breath-hold. The scanning direction was craniocaudal direction. Iodized contrast agent (350 mg I/mL, 1.5 mL/kg) was injected through a median cubital vein using a double-ended power syringe (injection speed 3.0 mL/s). Intelligent tracer was adopted in the arterial phase, and scanning starts promptly when CT value of the region of interest (ROI) placed on the abdominal aorta reached 180HU. The portal vein phase and the delayed phase were obtained 50–70 s and 90–120 s after the injection of contrast agent.

Volume of interest (VOI) segmentation and radiomics feature extraction

The workflow of our study was shown in Fig. 2. The VOIs segmentation was performed using 3D Slicer (version 4.13.0). Before segmentation, all the original images were imported into the software and standardized using a window width of 400 HU and a window level of 50 HU. Two radiologists with 5 and 10 years of experience, respectively, who were blind about the patient's clinical information, depicted the VOIs of gross lesions in portal venous phase as GLV. When there was multiple lesions

Table 1 Baseline patient characteristics in training and test cohorts

Characteristics	Training cohort			Test cohort		
	MVD positive ($n=144$)	MVD negative ($n=98$)	*p* value	MVD positive ($n=38$)	MVD negative ($n=23$)	*p* value
Age	37.22 ± 12.58	39.06 ± 13.54	0.272	37.29 ± 12.54	44.30 ± 14.41	0.056
BMI	22.17 ± 3.45	21.93 ± 2.96	0.867	23.26 ± 4.45	22.30 ± 2.75	0.510
Diameter	12.51 ± 4.73	11.68 ± 4.99	0.146	13.19 ± 4.97	11.61 ± 3.32	0.225
Sex			0.529			0.924
Male	69	51		17	10	
Female	75	47		21	13	
Calcification type			< 0.001			0.025
I	8	28		4	9	
II	73	53		23	8	
III	63	17		11	6	
WBC			0.318			0.873
$\leq 9.5\times10^9$/L	130	92		36	22	
$> 9.5\times10^9$/L	14	6		2	1	
NE			0.885			0.123
$\leq 6.3\times10^9$/L	133	91		36	19	
$> 6.3\times10^9$/L	11	7		2	4	
Lym			0.353			0.715
$\leq 3.2\times10^9$/L	143	96		37	22	
$> 3.2\times10^9$/L	1	2		1	1	
PLT			0.211			0.259
≤ 350 g/L	123	89		35	19	
> 350 g/L	21	9		3	4	
Crea			0.524			0.873
≤ 110 μmol/L	141	97		36	22	
> 110 μmol/L	3	1		2	1	
TBIL			0.092			0.152
≤ 22 μmol/L	104	80		27	20	
> 22 μmol/L	40	18		11	3	
AST			< 0.001			0.044
≤ 59 U/L	94	83		23	18	
> 59 U/L	50	15		15	3	
ALT			0.169			0.206
≤ 72 U/L	110	82		30	21	
> 72 U/L	34	16		8	2	
Fib			0.003			0.008
≤ 4 g/L	122	67		35	15	
>4 g/L	22	31		3	8	

MVD, microvascular density; BMI, body mass index; WBC, white blood cells; NE, neutrophils count; Lym, lymphocyte count; PLT, platelet count; Crea, creatinine; TBIL, total bilirubin; AST, aspartate aminotransferase; ALT, alanine aminotransferase; Fib, fibrinogen

in the liver, the largest one would be selected. Using the function of dilation as the basis of GLV to expand 10 mm, 15 mm, and20 mm outward, which was recorded as $GPLV_{10mm}$, $GPLV_{15mm}$, and $GPLV_{20mm}$, respectively. The non-liver parenchyma was wiped with the eraser function. The radiomics features were extracted from each VOI using open-source Pyradiomics (version 3.0.1, https://pyradiomics.readthedocs.io/en/latest/index.html) toolbox and processed using Scikit-learn (version 1.0.2, https://scikit-learn.org/stable/index.html) package. Images were resampled at a pixel size of 1 mm×1 mm×1 mm before feature extraction. Radiomics features included first-order features, shape features, gray level co-occurrence matrix features (GLCM), gray level size zone matrix features (GLSZM), gray level run length matrix features (GLRLM), neighbouring gray tone difference matrix features (NGTDM), and gray level dependence matrix features (GLDM). In addition, a variety of filters, such as the wavelet, Laplacian of Gaussian filter (LoG), logarithm, exponential, gradient, square, square root, local binary pattern 2D, local binary pattern 3D, were used to

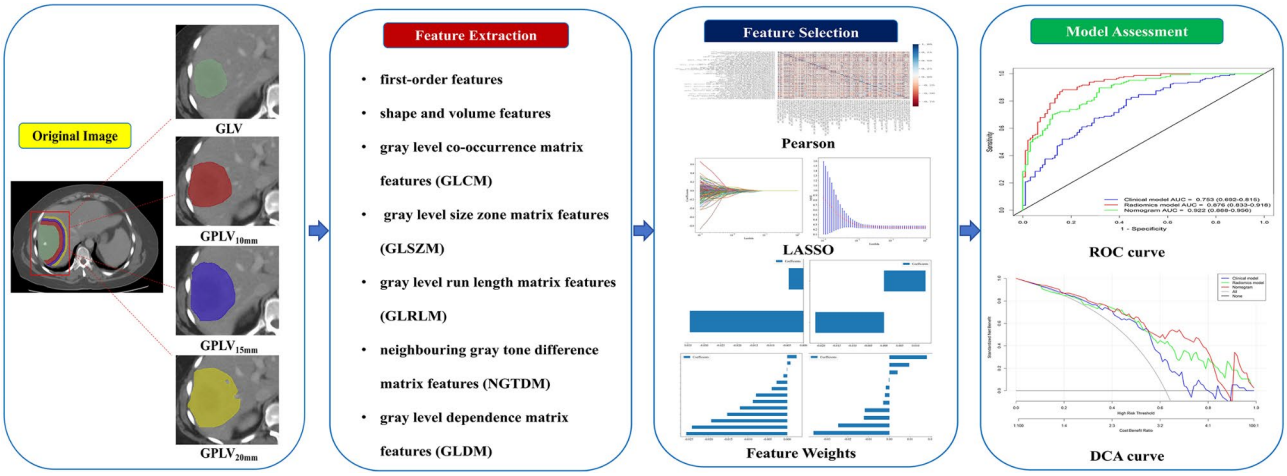

Fig. 2 Workflow of rasdiomic analysis in this study

calculate the first-order statistics and texture features of the transformed images.

Radiomics feature selection and model construction

The radiomics features were standardized using z-score normalization. Interclass and intraclass correlation coefficients (ICCs) were calculated to evaluate the inter-observer and intra-observer agreement for the radiomics features. An ICC > 0.75 of features were considered good and forwarded to the further feature selection. Then the Pearson correlation coefficient > 0.9 was utilized to handle strong correlations between features. To further refine the features, the multivariate least absolute shrinkage and selection operator (LASSO) regression was employed. A 10-fold cross-validation was used to determine the best lambda values to minimize the prediction error. The selected features were subsequently used to develop predictive models using five machine learning algorithms: logistic regression (LR), support vector machine (SVM), random forest (RF), extremely randomized trees (ExtraTrees), and extreme gradient boosting (XGBoost). To ensure the stability and robustness of model performance, a 10-fold cross-validation procedure was repeated over 100 iterations. The classifier with the highest mean area under the curve (AUC) across all iterations was selected as the optimal model.

Nomogram construction

The nomogram based on the logistic regression were constructed with the signature of the best radiomics model and the clinical signature. In addition, the nomogram determined the risk of the MVD by summing the points corresponding to all predictors to facilitate prediction. It provided a direct and visual representation of the assessment for the MVD of HAE.

Statistical analysis

Statistical analyses were performed using R software (version 4.2.2; http://www.R-project.org), and two-side p-values < 0.05 were considered statistically significant. Clinical information was expressed as mean ± standard deviations (SD) or number (frequency). Chi-square test was used for categorical variables. The ICC value of concordance was used to measure the degree of agreement between the two experienced radiologists. The independent predictors of the MVD of HAE were determined by univariable and multivariable logistic regression analysis. The ROC was drawn to evaluate the performance of the model, and difference in AUC was assessed with DeLong test. The DCA curve was used to evaluate the clinical benefit of the models.

Results

Patient characteristics

A total of 303 patients (male/female: 147/156, aged: 38.36 ± 13.11 years) were included (MVD positive, n = 182; MVD negative, n = 121). The flowchart of patients enrolled was shown in Fig. 1. The training and test cohort included 242 and 61 patients, respectively. Baseline patient characteristics in training and test cohorts were shown in Table 1. There were no statistically significant differences in age, sex, BMI, diameter of lesion, WBC, NE, Lym, PLT, Crea, TBIL, ALT and Fib between MVD positive and negative in both training cohort and test cohort (all p > 0.05). Univariate and multivariate logistic regressions showed that calcification type, AST and Fib could be used as independence predictors of MVD positive in HAE(p < 0.05) (Table 2).

Radiomics feature selection

A total of 1874 radiomics features were extracted from the four VOIs, respectively. The consistency of radiomics features calculated by two radiologists was above 0.90.

Table 2 Logistic regression analysis of clinical factors of patients in the training cohort

Parameters	Univariate analysis		Multivariate analysis	
	OR (95% CI)	*p* value	OR (95% CI)	*p* value
Age	0.989 (0.970–1.009)	0.279		
BMI	1.023 (0.945–1.108)	0.576		
Diameter	1.037 (0.982–1.095)	0.188		
Sex	1.179 (0.706–1.972)	0.529		
Calcification	3.393 (2.162–5.326)	< 0.001	3.220 (2.011–5.157)	< 0.001
WBC	1.004 (0.942–1.070)	0.908		
NE	0.965 (0.825–1.128)	0.654		
Lym	1.227 (0.835–1.824)	0.312		
PLA	1.001 (0.998–1.004)	0.398		
Crea	0.996 (0.981–1.011)	0.609		
TBIL	1.006 (0.994–1.018)	0.335		
AST	1.016 (1.008–1.025)	< 0.001	1.015 (1.006–1.024)	0.001
ALT	1.002 (0.999–1.005)	0.269		
Fib	0.649 (0.451–0.934)	0.019	0.645 (0.439–0.947)	0.014

BMI, body mass index; WBC, white blood cells; NE, neutrophils count; Lym, lymphocyte count; PLT, platelet count; Crea, creatinine; TBIL, total bilirubin; AST, aspartate aminotransferase; ALT, alanine aminotransferase; Fib, fibrinogen

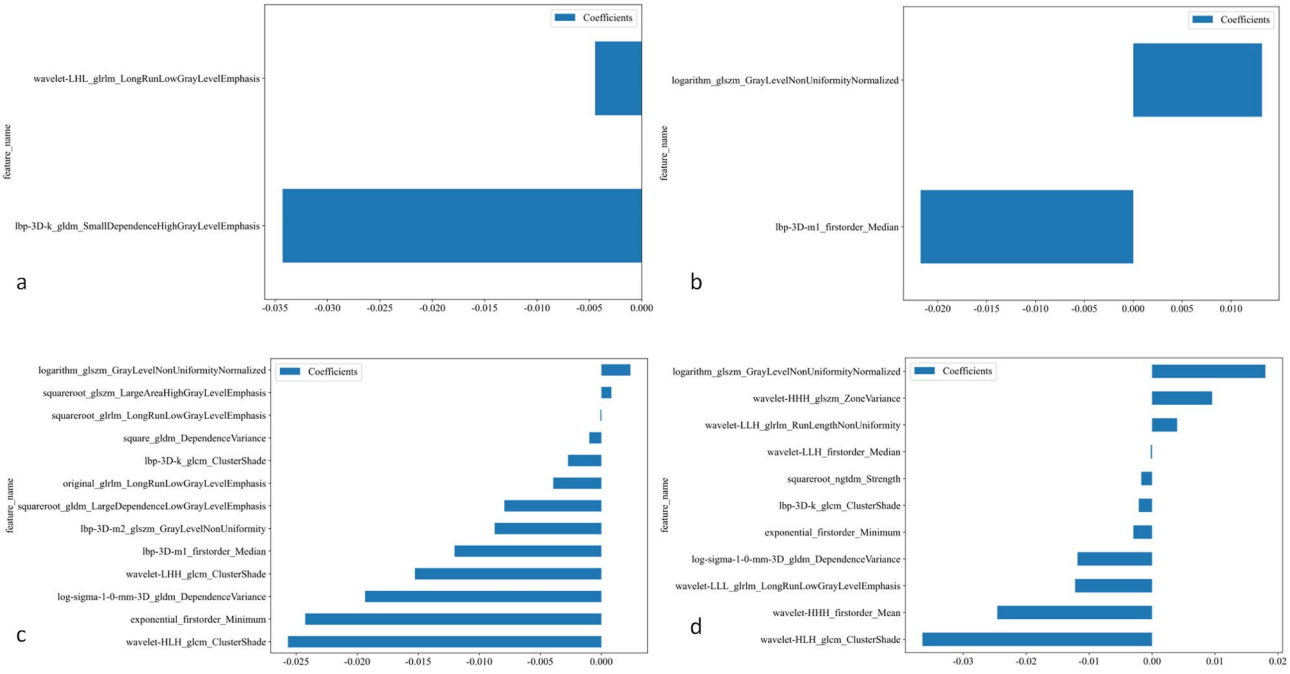

Fig. 3 Selected features weight coefficients. (**a**) GLV, (**b**) $GPLV_{10mm}$, (**c**) $GPLV_{15mm}$, (**d**) $GPLV_{20mm}$. GLV, gross lesion volume; $GPLV_{10mm}$, gross combined 10 mm perilesional volume; $GPLV_{15mm}$, gross combined 15 mm perilesional volume; $GPLV_{20mm}$, gross combined 20 mm perilesional volume

Pearson correlation coefficient greater than 0.90 were considered redundant and removed, leaving 364 features for GLV, 342 for $GPLV_{10mm}$, 346 for $GPLV_{15mm}$, and 349 for $GPLV_{20mm}$. After further dimension reduction by LASSO, the remaining features of the 4 VOIs were 2, 2, 13 and 11, respectively (Fig. 3).

Radiomics model construction and assessment

As shown in Table 3, the comparison of different algorithms across the four VOI models revealed that the model constructed using the ExtraTrees algorithm achieved a higher AUC in the test cohort compared to models built with other algorithms. It also demonstrated relatively better performance in terms of ACC values. The difference value in AUC of ExtraTrees algorithm between the training cohort and the test cohort was the smallest, indicating that the model was relatively stable. Figure 4 summarized the AUCs of the four VOIs in the training and test cohort. The AUC of GLV, $GPLV_{10mm}$, $GPLV_{15mm}$, and $GPLV_{20mm}$ in the training cohort were 0.699 (95%CI, 0.633–0.765), 0.711 (95%CI, 0.645–0.776), 0.806 (95%CI, 0.750–0.861), and 0.876 (95%CI,

Table 3 Comparison of models constructed by different algorithms based on $GPLV_{20mm}$ optimal features

algorithms	Training cohort					Test cohort				
	AUC(95% CI)	ACC	SEN	SPE	F1	AUC(95% CI)	ACC	SEN	SPE	F1
LR	0.654(0.585–0.723)	0.620	0.625	0.612	0.662	0.776(0.657–0.894)	0.738	0.895	0.478	0.810
SVM	0.856(0.805–0.906)	0.773	0.694	0.888	0.784	0.760(0.634–0.886)	0.689	0.605	0.826	0.708
RF	0.856(0.805–0.906)	0.810	0.875	0.714	0.846	0.770(0.644–0.896)	0.721	0.737	0.696	0.767
ExtraTrees	0.876(0.833–0.918)	0.806	0.889	0.684	0.845	0.802(0.690–0.914)	0.721	0.711	0.739	0.761
XGBoost	0.852(0.804–0.899)	0.760	0.708	0.837	0.779	0.746(0.623–0.869)	0.607	0.395	0.957	0.556

LR, logistic regression; SVM, support vector machine; RF, random forest; ExtraTrees, Extremely randomized trees; XGBoost, Extreme Gradient Boosting; AUC, area under the curve; ACC, accuracy; SEN, sensitivity; SPE, specificity

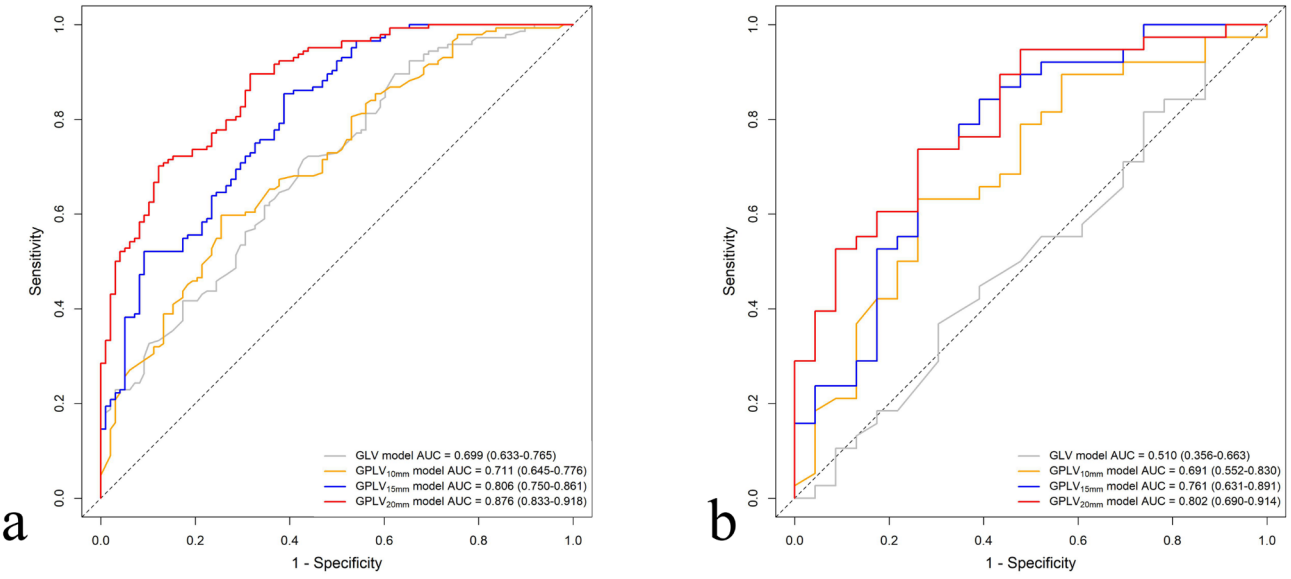

Fig. 4 AUCs of the four VOIs in the training and test cohort. (**a**) Training cohort, (**b**) Test cohort. AUC, area under the curve; VOI, volume of interest

0.833–0.918), respectively. The AUC of GLV, $GPLV_{10mm}$, $GPLV_{15mm}$, and $GPLV_{20mm}$ in the test cohort were 0.510 (95%CI, 0.356–0.633), 0.691 (95%CI, 0.552–0.830), 0.761 (95%CI, 0.631–0.891), and 0.802 (95%CI, 0.690–0.914), respectively. The $GPLV_{20mm}$ radiomics model had the best predicted performance among the four VOIs.

Nomogram performance testing

The Nomogram was constructed by combining the $GPLV_{20mm}$ radiomics model with clinical signature (Fig. 5). Figure 6a showed the AUCs of three models, in training cohort, the AUCs of clinical model, $GPLV_{20mm}$ radiomics model, and the nomogram were 0.753 (95%CI, 0.692–0.815), 0.876 (95%CI, 0.833–0.918), 0.922 (95%CI, 0.888–0.956), respectively. As shown in Fig. 6b, the nomogram still performed the highest AUC among the three models in the test cohort, it was 0.849 (95%CI, 0.750–0.947), and the clinical model and $GPLV_{20mm}$ radiomic model were 0.699 (95%CI, 0.553–0.845), 0.802 (95%CI, 0.690–0.914), respectively. The DeLong test showed that the AUC of monogram was significantly different from the other two models. As shown by decision DCA curves (Fig. 6c-d), nomogram exhibited increased clinical benefit in both training cohort and test cohort.

Discussion

This retrospective study extracted perilesional radiomics features from a 0–20 mm range to uncover new insights of the lesion evaluation. The results showed that CT-based radiomics model which constructed by intralesional and 20 mm perilesional region of HAE performed best among the models of four different VOIs, and the nomogram constructed with the radiomic signature and clinical signature shown the highest application value in predicting the MVD of HAE. This is the first study to investigate the performance of radiomics models with different perilesional scales including the 0–20 mm region for predicting the MVD and bioactivity of HAE, and it provided a better understand the infiltration width and safe distance of HAE.

HAE, often referred to as "worm cancer", exhibits a growth pattern similar to that of liver cancer [15]. Further clinical intervention is based on the peripheral infiltration zone and the bioactivity of HAE [16]. Previous studies have shown that MVD in the infiltration zone

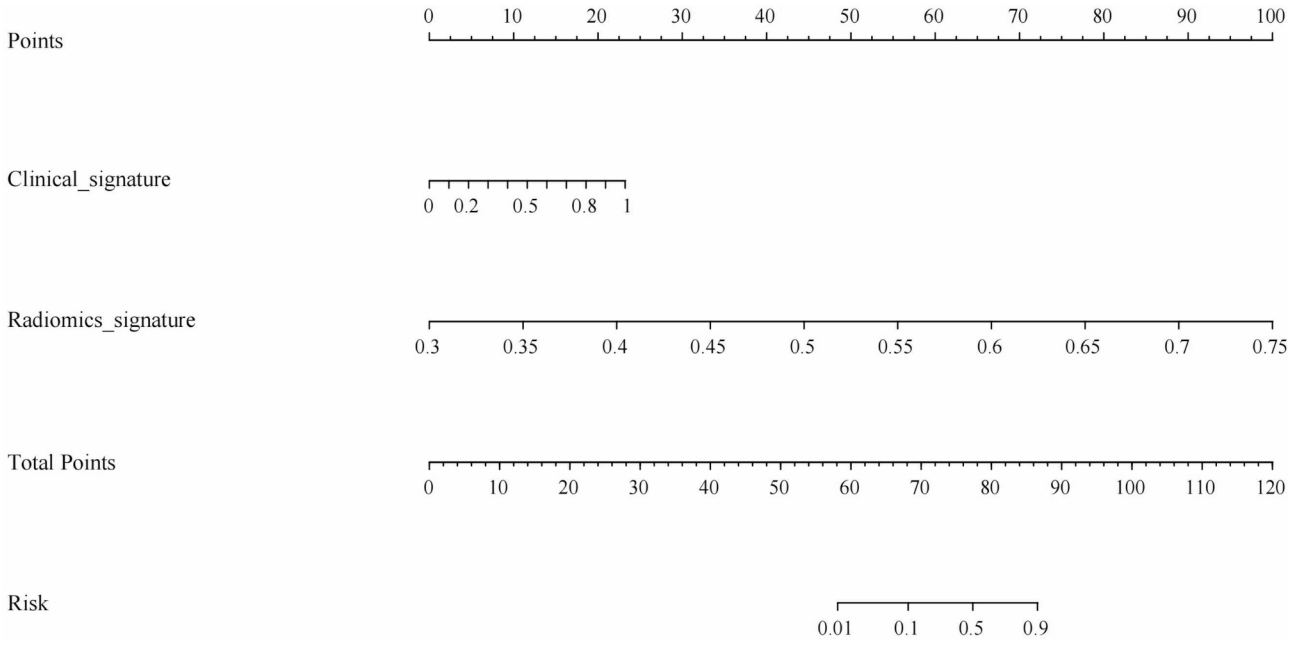

Fig. 5 Nomogram

of HAE lesions serves as the foundation for their proliferation and development, making it a gold standard for assessing bioactivity [5]. Therefore, preoperative noninvasive assessment of MVD in HAE remains a major clinical challenge. In addition, HAE has a tendency to invade neighboring tissues, which is surrounded by macrophages, lymphocytes, and fibrocytes, and forms granuloma tissues resembling a malignant tumor [17, 18]. The width of its outward invasion is also an important basis for surgical margin. Hillenbrand et al. [19] proposed that long-term disease-free survival in all patients required a safe distance of at least 20 mm provides. From the series of studies of Buttenschoen et al. [20], once the pathologist measured a macroscopic circular minimal safe distance of 17 mm, the microscopic one was only 2 mm. Therefore, they agreed with the view of 20 mm safe distance in previous studies. A study from China has shown that a safe distance of at least 1 mm in combination with medical anthelmintic treatment continuing for two years might offer a good chance of being disease-free long term, but the exact period of medical treatment needed is not defined [19]. Therefore, the width of the marginal infiltration zone is another key factor for clinicians. However, we found that the performance of clinical model in predicting the MVD of HAE was unsatisfactory (training cohort, AUC = 0.753; test cohort, AUC = 0.699).

Radiomics aims to describe and predict the ultrastructural architecture of tumors by analyzing medical images, with the potential to transform radiological tests into virtual biopsies [21]. Machine learning is a scientific discipline focused on how computers learn from data and plays a core technology to achieve artificial intelligence [22]. As radiomics methods and machine learning continue to be applied in the study of various clinical diseases, researchers have begun to explore the feasibility of radiomics in the diagnosis, differentiation, and bioactivity prediction of echinococcosis [9, 10, 23, 24]. Although studies on intralesional radiomics models have achieved certain prediction performance, while are still not accurate and comprehensive. In this study, we first compared the performance of five common machine learning algorithms in predicting the MVD of HAE. The result showed that the ExtraTrees algorithm outperformed the others. The ExtraTrees algorithm is an ensemble method based on the Decision Tree. By dividing completely random features and thresholds, it enhances the diversity of Decision Tree, with reducing over-dependence on specific features in the prediction, which could improve the model robustness and mitigate overfitting. Compared with the machine learning algorithms used in previous studies, it also demonstrates good stability.

The 10 mm range of perilesional radiomics features has been shown to have better predictive efficacy than GLV and clinical models in predicting bioactivity of HAE [25]. However, the maximum range of the edge extracted in previous study was 10 mm. In this study, we extended the range of the VOI to 20 mm, which was recognized as an operational safe distance in clinical practice. Meanwhile, we analyzed radiomics feature models for different VOIs within 10–20 mm margin of the lesion to further explore heterogeneity of the HAE margin zone. The results showed that the $GPLV_{20mm}$ model exhibited the best diagnostic performance among the four different radiomics models, with the AUCs of the training cohort

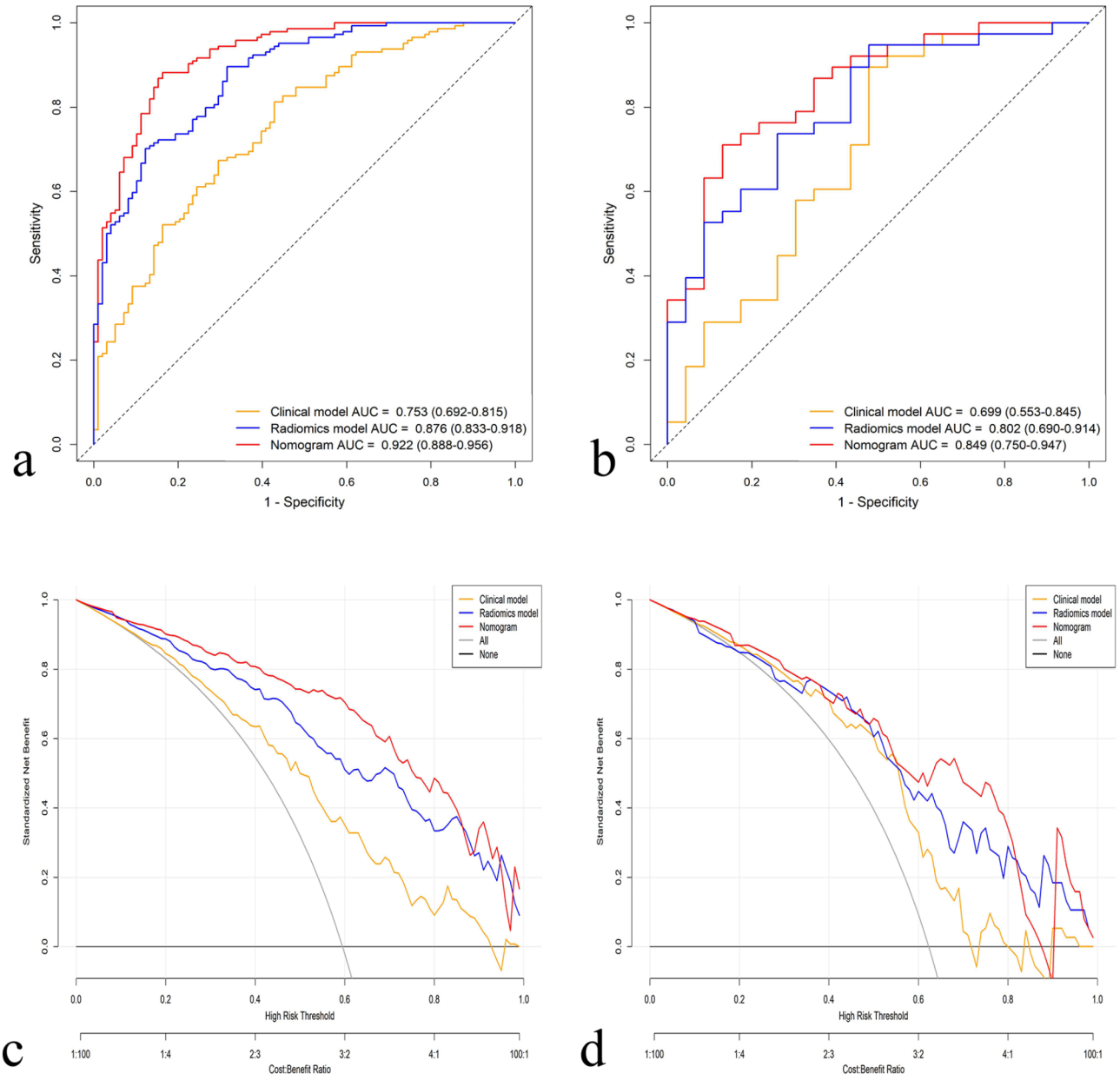

Fig. 6 The ROC and DCA curves of the three models for predicting the MVD of HAE. (**a**-**b**) ROC in training cohort and test cohort, (**c**-**d**) DCA curves in training cohort and test cohort. ROC, receiver operating characteristic Curve; DCA, decision curve analysis

and test cohort were 0.876, 0.802, respectively. The radiomics features including the surrounding 20 mm of HAE lesion may better predict the MVD of HAE. Additionally, the AUC of $GPLV_{10mm}$ model were higher than that of the GLV model, which was consistent with the results of previous study. Overall, we can infer that there is still heterogeneity in the tissue surrounding the lesion within 20 mm, which better reflects its peripheral infiltration zone and bioactivity, and also supports the previous clinical finding that the minimum safe distance for HAE radical resection is 20 mm [3].

The study further integrated clinical signature and imaging signature to construct a visual nomogram model. Compared with the clinical model or radiomics model, the nomogram demonstrated the best prediction performance and clinical benefit. The nomogram model, which was more comprehensive and accurate, could provide a reliable individualized basis for the selection of treatment strategies and the evaluation of efficacy of HAE. In recent years, the deep learning technique has also been well applied in various systems of systemic diseases. Two multicenter studies from China have realized automatic identification and classification of HAE using

the deep learning-based algorithms with CT plain scan and ultrasound images, respectively [26, 27]. These provided a new inspiration for further studies on the bioactivity and microenvironment of HAE.

Our study still had several limitations. First, it is a single-center study, and this study excluded patients with poor image quality or other treatments were excluded, potentially resulting in selection bias and decreasing the reliability of our study's conclusions. Second, the correlation between MVD and survival prognosis of HAE has not been investigated. Thirdly, in this study, only radiomics features were extracted for analysis and modeling. In future studies, we will further investigate the heterogeneity and survival prognosis of HAE microenvironment using deep learning and habitat analysis.

Conclusions

CT-based radiomics model which constructed by intralesional and 20 mm perilesional region of HAE was the best radiomics model for predicting its MVD, the nomogram model combined the clinical and radiomics signatures showed the best predictive performance.

Abbreviations

ALT	Alanine aminotransferase
AST	Aspartate aminotransferase
AUC	Area under the curve
BMI	Body mass index
CEUS	Contrast-enhanced ultrasound
Crea	Creatinine
CT	Computed tomography
DCA	Decision curve analysis
ExtraTrees	Extremely randomized trees
FDG-PET	Fluorodeoxyglucose positron-emission tomography
Fib	Fibrinogen
GLCM	Gray level co-occurrence matrix features
GLDM	Gray level dependence matrix features
GLRLM	Gray level run length matrix features
GLSZM	Gray level size zone matrix features
GLV	Gross lesion volume
$GPLV_{10mm}$	Gross combined 10 mm perilesional volume
$GPLV_{15mm}$	Gross combined 15 mm perilesional volume
$GPLV_{20mm}$	Gross combined 20 mm perilesional volume
HAE	Hepatic alveolar echinococcosis
ICC	Intraclass correlation coefficients
LASSO	Least absolute shrinkage and selection operator
LR	Logistic regression
Lym	Lymphocyte count
MVD	Microvessel density
NE	Neutrophils count
NGTDM	Neighbouring gray tone difference matrix features
PLT	Platelet count
RF	Random forest
ROC	Receiver operating characteristic curve
SVM	Support vector machine
TBIL	Total bilirubin
VOI	Volume of interest
WBC	White blood cells
XGBoost	Extreme Gradient Boosting

Supplementary Information

The online version contains supplementary material available at https://doi.org/10.1186/s12880-025-01612-5 .

Supplementary Material 1

Supplementary Material 2

Acknowledgements

Not applicable.

Author contributions

All authors contributed to the study conception and design. Material preparation, data collection were performed by Juan Hou, Simiao Zhang, Shouxian Li, Tieliang Zhang. Data analysis were performed by Zicheng and Zhao Longfei. The first draft of the manuscript was written by Juan Hou and all authors commented on previous versions of the manuscript. Wenya Liu provided logistical and administrative support, ensured compliance with ethical standards, and reviewed and approved the manuscript for submission. All authors reviewed the manuscript.

Funding

This study was supported by the National Natural Science Foundation of China (81974263).

Data availability

The data that support the findings fo this study ara available form First Affiliated Hospital of Xinjiang Medical University but restrictions apply to the availablility of theae data, which were used under license for the current study, and so are not publicly available. Data are however available from the corresponding author on reasonable request and with the permission of First Affiliated Hospital of Xinjiang Medical University.

Declarations

Ethical approval

This retrospective study was approved by the institutional Ethics Committee of the First Affiliated Hospital of Xinjiang Medical University (No. K202312-38), and was conducted in accordance with the 1964 Helsinki Declaration and its later amendments or comparable ethical standards. Patient informed contents were waived.

Consent for publication

Not applicable.

Competing interests

The authors declare no competing interests.

Received: 14 December 2024 / Accepted: 24 February 2025
Published online: 10 March 2025

References

1. Baumann S, Shi R, Liu W, et al. Worldwide literature on epidemiology of human alveolar echinococcosis: a systematic review of research published in the twenty-first century[J]. Infection. 2019;47(5):703–27. https://doi.org/10.1007/s15010-021-01695-6
2. Ma T, Wang Q, Hao M, et al. Epidemiological characteristics and risk factors for cystic and alveolar echinococcosis in China: an analysis of a national population-based field survey[J]. Parasites Vectors. 2023;16(1):181. https://doi.org/10.1186/s13071-023-05788-z
3. Vuitton DA, Azizi A, Richou C, et al. Current interventional strategy for the treatment of hepatic alveolar echinococcosis[J]. Expert Rev Anti-infective Therapy. 2016;14(12):1179–94. https://doi.org/10.1080/14787210.2016.1240030
4. Brumpt E, Blagosklonov O, Calame P, et al. AE hepatic lesions: correlation between calcifications at CT and FDG-PET/CT metabolic activity[J]. Infection. 2019;47(6):955–60. https://doi.org/10.1007/s15010-019-01328-z
5. AJD, Chai JP, Zhao SY, et al. Research progress on infiltrating zone and microvascular invasion of hepatic alveolar echinococcosis[J]. Chin J Prev Med. 2022;56(10):1514–9. https://doi.org/10.3760/cma.j.cn112150-20211118-01062

6. Jiang Y, Li J, Wang J, et al. Assessment of vascularity in hepatic alveolar echinococcosis: comparison of quantified dual-energy CT with histopathologic parameters[J]. PLoS ONE. 2016;11(2):e0149440. https://doi.org/10.1371/journal.pone.0149440
7. Jing Y, Jun-Hu B, Yong-Hai Z, et al. Revolution CT hepatic perfusion imaging assessment of peripheral infiltration zone of hepatic alveolar echinococcosis[J]. Zhongguo Xue Xi Chong Bing Fang Zhi Za zhi = Chinese. J Schistosomiasis Control. 2019;30(6):678–81. https://doi.org/10.16250/j.32.1374.2018123
8. Yangdan C-R, Wang C, Zhang L-Q, et al. Recent advances in ultrasound in the diagnosis and evaluation of the activity of hepatic alveolar echinococcosis[J]. Parasitol Res. 2021;120(9):3077–82. https://doi.org/10.1007/s00436-021-07262-0
9. Li Y, Yu Y, Liu Q, et al. A CT-based radiomics nomogram for the differentiation of pulmonary cystic echinococcosis from pulmonary abscess[J]. Parasitol Res. 2022;121(12):3393–401. https://doi.org/10.1007/s00436-022-07663-9
10. Zhou Y, Feng P, Tian F, et al. A CT-based radiomics model for predicting lymph node metastasis in hepatic alveolar echinococcosis patients to support lymph node dissection[J]. Eur J Med Res. 2024;29(1):409. https://doi.org/10.1186/s40001-024-01999-x
11. Ren B, Wang J, Miao Z et al. Hepatic alveolar echinococcosis: predictive biological activity based on radiomics of MRI[J]. BioMed Research International. 2021;2021:6681092. https://doi.org/10.1155/2021/6681092
12. Wang X, Yang L, Chen L, et al. Evaluation of the metabolic activity of the infiltration and proliferation areas of hepatic alveolar echinococcosis in rats using contrast-enhanced ultrasound[J]. Am J Trop Med Hyg. 2022;107(6):1185–9. https://doi.org/10.4269/ajtmh.22-0348
13. Weidner N. Current pathologic methods for measuring intratumoral microvessel density within breast carcinoma and other solid tumors[J]. Breast Cancer Res Treat. 1995;36(2):169–80. https://doi.org/10.1007/BF00666038
14. Song T, Li H-T, Yang L-F, et al. [Contrast-enhanced ultrasonography of hepatic alveolar echinococcosis in rats: the correaltion of imaging fratures and histologic microvascular density][J]. Zhongguo Ji Sheng Chong Xue Yu Ji Sheng Chong Bing Za zhi = Chinese. J Parasitol Parasitic Dis. 2014;32(3):200–4.
15. Joliat G-R, Martins-Filho SN, Haefliger S, et al. Programmed death-ligand1 is a determinant of recurrence in alveolar echinococcosis[J]. Int J Infect Dis. 2023;129:285–8. https://doi.org/10.1016/j.ijid.2023.01.043
16. Kamiyama T. Recent advances in surgical strategies for alveolar echinococcosis of the liver[J]. Surg Today. 2020;50(11):1360–7. https://doi.org/10.1007/s00595-019-01922-6
17. Jiang T, Aji T, Ran B, et al. Collateral circulation caused by end-stage hepatic alveolar echinococcosis[J]. BMC Infect Dis. 2023;23(1):1–8. https://doi.org/10.1186/s12879-022-07970-7
18. McManus DP, Zhang W, Li J, et al. Echinococcosis[J] Lancet. 2003;362(9392):1295–304. https://doi.org/10.1016/S0140-6736(03)14573-4
19. Hillenbrand A, Gruener B, Kratzer W, et al. Impact of safe distance on long-term outcome after surgical therapy of alveolar Echinococcosis[J]. World J Surg. 2017;41(4):1012–8. https://doi.org/10.1007/s00268-016-3813-6
20. Buttenschoen K, Carli Buttenschoen D, Gruener B, et al. Long-term experience on surgical treatment of alveolar echinococcosis[J]. Langenbeck's Archives Surg. 2009;394(4):689–98. https://doi.org/10.1007/s00423-008-0392-5
21. Ferrari R, Trinci M, Casinelli A, et al. Radiomics in radiology: what the radiologist needs to know about technical aspects and clinical impact[J]. Radiol Med. 2024;129(12):1751–65. https://doi.org/10.1007/s11547-024-01904-w
22. Deo RC. Machine learning in medicine[J]. Circulation. 2015;132(20):1920–30. https://doi.org/10.1161/CIRCULATIONAHA.115.001593
23. Yimit Y, Yasin P, Tuersun A, et al. Differentiation between cerebral alveolar echinococcosis and brain metastases with radiomics combined machine learning approach[J]. Eur J Med Res. 2023;28(1):577. https://doi.org/10.1186/s40001-023-01550-4
24. Nijiati M, Tuerdi M, Damola M, et al. A deep learning radiomics model based on CT images for predicting the biological activity of hepatic cystic echinococcosis[J]. Front Physiol. 2024;15:1426468. https://doi.org/10.3389/fphys.2024.1426468
25. Zhang S, Hou J, Xia W, et al. Value of intralesional and perilesional radiomics for predicting the bioactivity of hepatic alveolar echinococcosis[J]. Front Oncol. 2024;14. https://doi.org/10.3389/fonc.2024.1389177
26. Yang Y, Cairang Y, Jiang T, et al. Ultrasound identification of hepatic echinococcosis using a deep convolutional neural network model in China: a retrospective, large-scale, multicentre, diagnostic accuracy study[J]. Lancet Digit Health. 2023;5(8):e503–14. https://doi.org/10.1016/S2589-7500(23)00091-2
27. Wang Z, Bian H, Li J, et al. Detection and subtyping of hepatic echinococcosis from plain CT images with deep learning: a retrospective, multicentre study[J]. Lancet Digit Health. 2023;5(11):e754–62. https://doi.org/10.1016/S2589-7500(23)00136-X

Publisher's note